Bull. Chem. Soc. Ethiop. **2026**, 40(12), 2577-2595. ISSN 1011-3924
© 2026 Chemical Society of Ethiopia and The Authors Printed in Ethiopia
DOI: https://dx.doi.org/10.4314/bcse.v40i12.6 Online ISSN 1726-801X

SYNTHESIS, STRUCTURAL AND ELECTRONIC CHARACTERIZATION OF [Mn(4-OHBA)$_3$(MEA)(H$_2$O)]Cl$_2$ COMPLEX: A COMBINED EXPERIMENTAL AND COMPUTATIONAL STUDY

Matluba Yadgarova[1], Mansur Ashirov[1], Shodlik Khasanov[1], Nodira Obidova[2], Khushnudbek Eshchanov[3], Ikram Abdullaev[1], Oybek Khudoyberganov[1*], Sapajan Ibragimov[1,4*]

[1]Department of Exact Science, Khorezm Mamun Academy, Khiva, Uzbekistan
[2]Physical Education and Sports Department, Tashkent Institute of Irrigation and Agricultural Mechanization Engineers National Research University, Tashkent, Uzbekistan
[3]Department of Chemistry, Urganch State University, Urgench, Uzbekistan
[4]Faculty of Chemistry, Gdansk University of Technology, Gdańsk, Poland

(Received April 30, 2026; Revised August 25, 2026; Accepted September 3, 2026)

ABSTRACT. A mononuclear manganese(II) coordination compound of composition [Mn(4-OHBA)$_3$(MEA)(H$_2$O)]Cl$_2$ (4-OHBA = 4-hydroxybenzamide, MEA = monoethanolamine) has been synthesized and characterized by infrared spectroscopy, scanning electron microscopy with energy-dispersive X-ray analysis, X-ray powder diffraction, and density functional theory. Diffraction data collected in Gandolfi geometry and analyzed by Rietveld refinement, indexed on a triclinic cell in space group P-1, are consistent with a mononuclear complex in which the manganese center adopts a distorted octahedral N$_4$O$_2$ donor environment provided by three amide ligands, a chelating aminoalcohol and a coordinated water molecule, with chloride ions in the outer coordination sphere. Density functional theory calculations establish a high-spin sextet ground state, characterize the frontier orbitals and electronic transitions of the complex, and yield global reactivity descriptors indicating moderate chemical hardness together with appreciable electrophilic character. Molecular docking against human apurinic/apyrimidinic endonuclease 1, a base-excision-repair enzyme that is frequently overexpressed in human cancers and associated with resistance to chemotherapy, predicts favorable binding within the enzyme active site. These predictions are computational and require experimental validation.

KEY WORDS: Manganese(II) complex, 4-hydroxybenzamide, Monoethanolamine, Mixed-ligand coordination compound, X-ray powder diffraction, Density functional theory

INTRODUCTION

Manganese is distinguished among the transition metals by its wide range of accessible oxidation states, from Mn(II) to Mn(VII), and by the corresponding richness of its coordination chemistry. Its most prominent biological role is found in Photosystem II, where the oxygen-evolving complex — a Mn$_4$CaO$_5$ cluster — catalyzes the oxidation of water to molecular oxygen, the oxido bridges between the manganese ions playing a decisive part in electron transfer [1, 2]. Beyond photosynthesis, manganese serves as an essential cofactor in redox enzymes such as manganese superoxide dismutase and manganese catalase, which detoxify reactive oxygen species in living systems [3, 4]; synthetic small-molecule mimics of these enzymes have themselves been investigated as therapeutic agents [5].

The structural and magnetic diversity of manganese coordination compounds has been explored extensively, encompassing mononuclear, polynuclear and polymeric architectures assembled from oxime, carboxylate and related ligand systems [6-11]. These biological functions and structural possibilities have together inspired sustained interest in synthetic manganese complexes as enzyme models and as candidate therapeutic agents, with reported activities spanning the anticancer, antimicrobial, antifungal and antioxidant domains [12-18]. The

*Corresponding authors. E-mail: oybekkhudoyberganov395@gmail.com, sapajan.ibragimov@pg.edu.pl
This work is licensed under the Creative Commons Attribution 4.0 International License

biological behavior of such complexes is strongly governed by ligand architecture, which modulates the redox properties, lipophilicity and cellular uptake of the metal center. Altered manganese homeostasis has itself been associated with malignancy, which adds further motivation for examining manganese compounds in an oncological context [19].

In this context, 4-hydroxybenzamide (4-OHBA) is an attractive ligand candidate. It is the primary amide of 4-hydroxybenzoic acid, a scaffold whose derivatives display a broad range of documented biological activities, including antimicrobial and growth-modulating effects [20-22]. The amide function provides both nitrogen and oxygen donor atoms, while the para-hydroxyl group offers additional hydrogen-bonding capability, so that the molecule is well suited to coordination with first-row transition metals. A structurally related mixed-ligand cadmium compound combining 4-hydroxybenzoic acid with monoethanolamine has been described previously [23], establishing that this ligand pairing is capable of forming discrete coordination compounds.

To enhance the biological potential of the metal center, a mixed-ligand strategy was adopted, combining 4-OHBA with a complementary co-ligand. Mixed-ligand manganese complexes have been reported to display activities exceeding those of their individual components, an effect attributed to the combined influence of the two ligand systems on the coordination environment [17,18]. Monoethanolamine was selected as the co-ligand because its amino and hydroxyl groups form a stable five-membered chelate ring, and because it introduces additional hydrogen-bonding functionality into the lattice.

Although a considerable number of manganese(II) complexes with carboxylate and Schiff-base ligands have been reported, mixed-ligand systems combining a simple aromatic primary amide with an amino alcohol remain comparatively unexplored, and no compound of the present composition appears in the crystallographic literature. The present study reports the synthesis of such a compound and pursues three objectives: to establish its composition and coordination environment by infrared spectroscopy, electron microscopy and X-ray powder diffraction; to characterize its electronic structure, ground-state multiplicity and chemical reactivity by density functional theory; and to assess, by molecular docking, whether the complex might plausibly interact with a DNA repair enzyme of interest in oncology, as a preliminary guide to subsequent experimental work.

EXPERIMENTAL

Synthesis

Manganese(II) chloride tetrahydrate (0.198 g, 1 mmol) was dissolved in a mixed solvent of 5 mL distilled water and 5 mL ethanol. Separately, 4-hydroxybenzamide (0.411 g, 3 mmol) was dissolved in 20 mL ethanol. Monoethanolamine (0.061 g, 1 mmol) was dissolved in 10 mL ethanol and the two ligand solutions were combined. The synthesis is summarized in Scheme 1. The combined ligand solution was added dropwise to the metal salt solution at 2 mL every 15 min, and the mixture was refluxed with continuous magnetic stirring at 60-70 °C for 2 h, the pH being maintained at 8.5 with an ammonium buffer. The mixture was then sonicated at 30 kHz for 10 min, filtered, and held in a thermostat at 30 °C to crystallize by slow evaporation. Colorless crystals were collected, washed with cold diethyl ether and dried in air.

Elemental (CHN) analysis and inductively coupled plasma determination of the manganese content could not be performed, as the material prepared was consumed during the characterization described below. The composition given here is therefore proposed on the basis of the spectroscopic, microscopic and diffraction evidence rather than established by independent bulk analysis.

The synthesis may be represented as:

$$MnCl_2{\cdot}4H_2O + 3(4\text{-OHBA}) + MEA \rightarrow [Mn(4\text{-OHBA})_3(MEA)(H_2O)]Cl_2 + 3H_2O$$

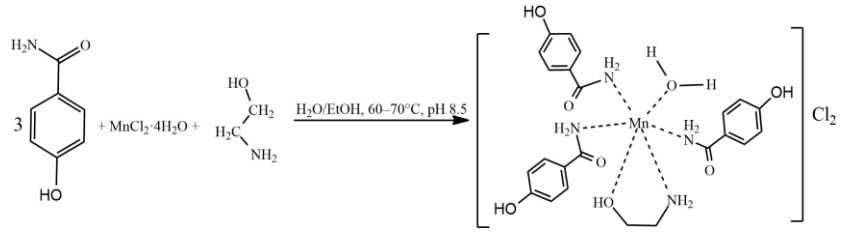

Scheme 1. Synthesis of $[Mn(4\text{-}OHBA)_3(MEA)(H_2O)]Cl_2$ from manganese(II) chloride tetrahydrate, 4-hydroxybenzamide and monoethanolamine, and the resulting N_4O_2 coordination environment.

X-ray diffraction measurement and structural modeling

Diffraction data were collected at 298 K on a Rigaku SmartLab diffractometer using Cu Kα radiation (λ = 1.54186 Å). Because only a small quantity of crystalline material was available, the sample was mounted in a capillary and measured using a Gandolfi attachment. In this geometry, the specimen is rotated simultaneously about two axes, so that the crystallites sample a wide range of orientations over the course of the exposure and a one-dimensional Debye–Scherrer powder pattern is obtained. Data were recorded from 5.0 to 60.0° 2θ in steps of 0.01° (5501 points).

The pattern was indexed on a triclinic cell with a = 10.950(4), b = 11.896(7), c = 10.00(18) Å, α = 100.93(3), β = 93.62(3), γ = 90.17(5)°, V = 1277(23) Å³. The centrosymmetric space group P-1 was assumed, with Z = 2. The number of Bragg reflections accessible within this range (735, to d_{min} = 1.54 Å) is far too small to permit independent refinement of the 38 non-hydrogen atomic positions of the asymmetric unit. A structural model was therefore constructed from the DFT-optimized molecular geometry and refined against the profile as a rigid body, together with the cell parameters, scale factor, background, peak-profile terms and a spherical-harmonic preferred-orientation correction of harmonic order 2, giving 42 refined parameters in total. Atomic displacement parameters were not refined. Hydrogen atoms were placed at calculated positions and were not refined. Rietveld refinement was carried out in SmartLab Studio II (Rigaku).

Refinement converged to R_p = 0.0404, R_{wp} = 0.0549, R_{exp} = 0.0439 and a goodness of fit (R_{wp}/R_{exp}) of 1.251, with a Bragg intensity residual R_I of 0.0089. Crystallographic data have been deposited with the Cambridge Crystallographic Data Center under deposition number CCDC 2575511. Structure factors are not available for a measurement of this type. The checkCIF/PLATON report is provided as Supporting Information.

The limitations of this procedure should be stated explicitly. The refinement establishes that the DFT-derived molecular model is compatible with the observed unit cell and diffraction profile; it does not constitute an independent experimental determination of the molecular geometry, and the two are therefore not independent sources of structural information. The bond lengths and angles reported in the structural section below are consequently calculated quantities and are quoted without experimental standard uncertainties. The agreement factors should likewise be interpreted with care. The profile residuals are computed over 5501 points, the majority of which describe background, while the Bragg residual rests on integrated intensities obtained by partitioning the observed profile according to the calculated model; in a triclinic cell with severe reflection overlap, this partitioning is itself model-dominated, so that the Bragg residual is not an independent test of the structure. Finally, because only a small number of microcrystals were available, particle statistics are poor, and a preferred-orientation correction was required. The molecular model presented here should accordingly be regarded as a proposal consistent with the available data rather than as a determined crystal structure.

RESULTS AND DISCUSSION

Infrared spectroscopy

Comparative infrared spectra of the complex and of its constituent starting materials are shown in Figure 1; assignments follow the conventions of Nakamoto [24].

The spectrum of free 4-hydroxybenzamide shows broad absorptions at 3432, 3348 and 3240 cm^{-1}, assigned to the phenolic ν(O–H) and to the symmetric and antisymmetric ν(NH_2) modes of the amide group. Their breadth reflects extensive intermolecular hydrogen bonding in the solid ligand. In the complex, the corresponding bands appear at 3427, 3348 and 3269 cm^{-1}, with altered profile and intensity. We attribute these changes to the coordinated water molecule, the hydroxyl group of monoethanolamine and the rearranged hydrogen-bonding network of the new lattice, rather than to coordination of the phenolic oxygen, which occupies the para position of the aromatic ring and cannot reach the metal centre.

The amide carbonyl stretch provides the most informative comparison. In the free ligand it appears at 1622 cm^{-1} and in the complex at 1666 cm^{-1}, a shift of +44 cm^{-1} to higher wavenumber. Coordination of a carbonyl oxygen to a metal center withdraws electron density from the C=O bond and lowers this frequency; the observed shift is in the opposite direction, and we therefore exclude coordination through the carbonyl oxygen. A shift to higher wavenumber is the behavior expected when the amide nitrogen donates its lone pair to the metal, since the nitrogen is thereby removed from conjugation with the carbonyl and the C=O bond acquires increased double-bond character.

Two qualifications should be entered. First, the value of 1622 cm^{-1} in the free ligand is low for a primary aromatic amide, which typically absorbs between 1650 and 1680 cm^{-1}, and reflects the strong hydrogen bonding evident in the ν(NH_2) region. Disruption of that hydrogen bonding on complexation would itself raise the carbonyl frequency towards the unassociated value, so the observed shift is consistent with amide-nitrogen coordination but does not establish it independently of that alternative. Second, the calculated geometry of the sextet ground state gives long Mn–N(amide) distances of 2.361-2.543 Å and a bond-valence sum of 1.54 at the metal, indicating a weak interaction. The infrared evidence excludes carbonyl-oxygen coordination; the strength and precise nature of the amide–metal interaction remain less well determined.

The amide II band and the aromatic ν(C=C) modes appear at 1573 and 1504 cm^{-1} in the free ligand and at 1574 and 1524 cm^{-1} in the complex, the latter with increased intensity. The shift in the amide II region, which contains ν(C–N) and δ(NH_2) character, is consistent with reduced electron density at the amide nitrogen on coordination. Intense bands between 1290 and 1010 cm^{-1} are assigned to ν(C–O) and ν(C–N) of monoethanolamine; their displacement relative to the free aminoalcohol is consistent with the N, O-bidentate chelation found in the structural model.

Bands at 852, 823, 787 and 747 cm^{-1} are characteristic of the out-of-plane C–H deformations of a para-disubstituted aromatic ring. Their retention shows that the aromatic framework is unaltered by complexation and that coordination proceeds through the donor functional groups rather than the ring.

Four bands at 607, 552, 530 and 430 cm^{-1} are absent from the spectra of the free ligands. These fall in the range commonly associated with metal–ligand stretching modes and are tentatively assigned to ν(Mn–O) and ν(Mn–N). Assignments in this region are not unambiguous, since ligand skeletal deformations also absorb here, and we do not treat these bands as independent proof of coordination.

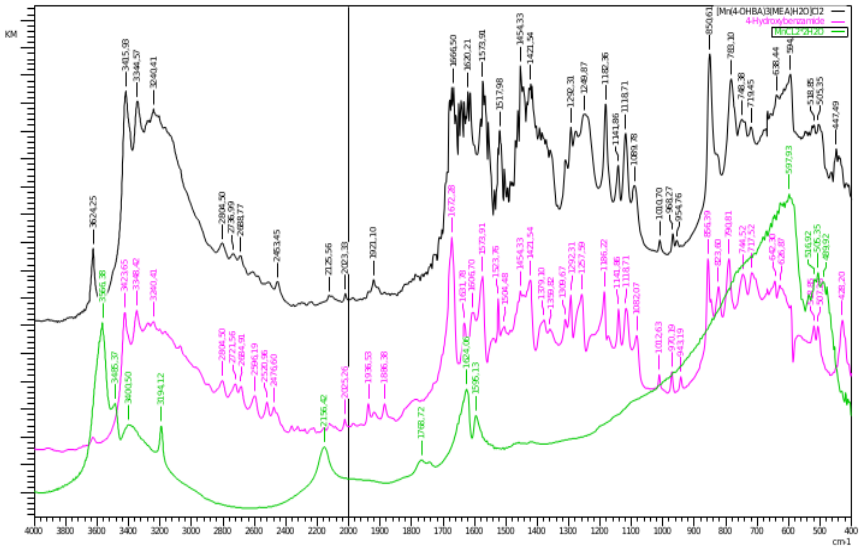

Figure 1. Comparative FTIR spectra of manganese(II) chloride tetrahydrate, free 4-hydroxybenzamide, monoethanolamine and $[Mn(4\text{-}OHBA)_3(MEA)(H_2O)]Cl_2$.

Scanning electron microscopy and energy-dispersive X-ray spectroscopy

Scanning electron microscopy (Figure 2a) revealed well-defined crystals of needle-like to rod-shaped habit, with smooth facets and sharp edges. Individual crystallites ranged from approximately 50 to 500 μm in length and from 20 to 100 μm in width.

Energy-dispersive X-ray spectroscopy was used to survey the elemental composition of the material. The spectrum (Figure 2b) shows peaks attributable to manganese (Mn-K, ~5.9 and ~6.5 keV), chlorine (Cl-K, ~2.6 keV), oxygen (O-K, ~0.5 keV), nitrogen (N-K, ~0.4 keV) and carbon (C-K, ~0.3 keV). The presence of these elements is consistent with the proposed formulation. We note, however, that the C-K, N-K and O-K lines lie close together and overlap substantially, so that quantification of the light elements by this technique is not reliable; the spectrum is therefore taken as qualitative evidence for the presence of these elements rather than as a determination of stoichiometry. Elemental mapping (Figure 2c–e) shows manganese and chlorine distributed evenly across the imaged crystal faces, with no segregation resolvable at the length scale accessible to the method.

These observations are consistent with the proposed composition but do not establish it. Energy-dispersive X-ray spectroscopy is a surface-sensitive technique of limited spatial resolution and poor sensitivity to light elements, and it cannot demonstrate phase purity, bulk stoichiometry, or the absence of residual starting materials. Confirmation of the bulk composition would require elemental analysis, inductively coupled plasma determination of the manganese content, and powder diffraction of a bulk polycrystalline sample. As noted in the synthesis process, these measurements could not be performed because the material was consumed during characterization.

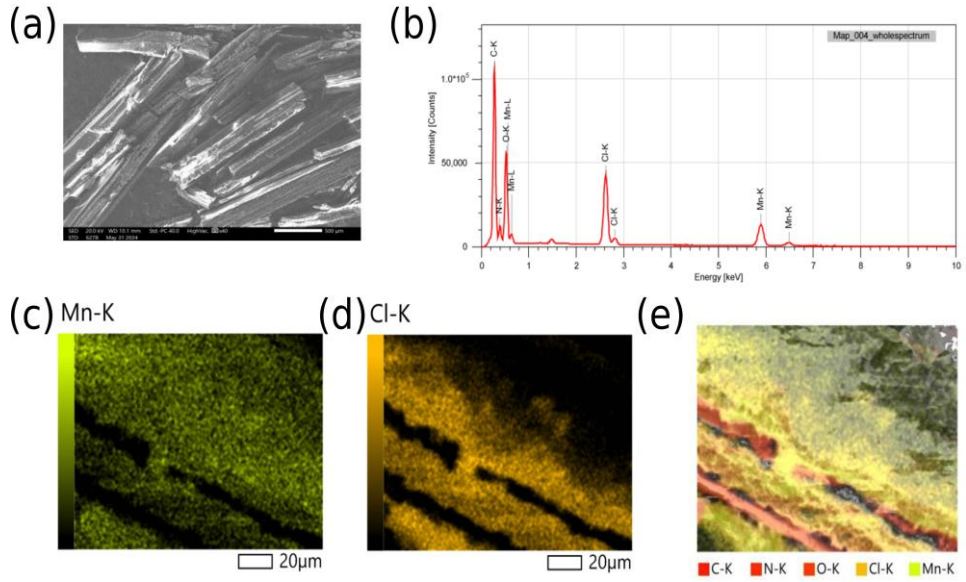

Figure 2. SEM-EDS characterization of $[Mn(4\text{-}OHBA)_3(MEA)(H_2O)]Cl_2$: micrograph of the crystal habit, EDS spectrum and elemental maps.

Computational methodology and optimized geometry

Quantum chemical calculations were performed using density functional theory as implemented in Gaussian 16 [25]. The complex was optimized at the TPSSh/Def2-SVP level with the CPCM continuum solvation model for water. The TPSSh hybrid meta-GGA functional [26,27] in combination with the Def2-SVP basis set [28] was selected for its established accuracy and computational efficiency in describing the geometric and electronic properties of first-row transition metal complexes [29]. Both chloride ions were included explicitly in the calculation, so that the system modelled is the neutral ion pair; the total charge was accordingly set to zero and the spin multiplicity to six for the high-spin d^5 ground state.

Since manganese(II) is a d^5 system capable of adopting several spin states, the doublet, quartet and sextet multiplicities were each examined in order to identify the ground-state configuration. Wave function stability was verified at the same level of theory.

The optimized geometry was confirmed to represent a true minimum on the potential energy surface by vibrational frequency analysis, no imaginary frequencies being obtained. The optimized structure comprises a manganese(II) center in a distorted octahedral N_4O_2 environment, coordinated by the amide nitrogen atoms of three 4-hydroxybenzamide ligands, by the amino nitrogen and hydroxyl oxygen of a chelating monoethanolamine molecule, and by one water molecule. The two chloride ions occupy the outer coordination sphere.

The energy differences between the doublet and sextet states, and between the quartet and sextet states, were 40.92 and 34.31 kcal mol^{-1} respectively. These substantial separations indicate that the sextet (S = 5/2) high-spin configuration is the thermodynamically preferred electronic state, as expected for the weak ligand field generated by nitrogen and oxygen donors [30-32]. The sextet and quartet solutions are essentially free of spin contamination, their $\langle S^2 \rangle$ values of 8.7550 and 3.7508 lying within 0.001 of the exact values. The doublet is appreciably contaminated (0.9363 against an exact 0.7500), so its energy should be regarded as the least reliable of the three; it is, however, far enough above the ground state that this does not affect the ordering.

Structural model from X-ray powder diffraction

The powder pattern was indexed on a triclinic cell (Table 1) of volume 1277 Å^3 with Z = 2, giving a calculated density of 1.60 g cm^{-3} and approximately 17 Å^3 per non-hydrogen atom. Both figures are typical of a molecular coordination compound of this composition and consistent with an extensively hydrogen-bonded lattice. A search of the Cambridge Structural Database returned no entry of comparable cell or composition, indicating that the compound has not previously been reported.

The molecular model refined against the profile is mononuclear (Figure 3). The manganese(II) center adopts a distorted octahedral N_4O_2 coordination environment assembled from three different ligand types. Monoethanolamine chelates through its amino nitrogen and hydroxyl oxygen, forming a five-membered ring with a bite angle of 80.28°; a coordinated water molecule completes the oxygen donor set; and the three 4-hydroxybenzamide ligands each bind through the nitrogen atom of the amide group. The two chloride ions occupy the outer coordination sphere, so that the complex ion is the dication $[Mn(4\text{-}OHBA)_3(MEA)(H_2O)]^{2+}$ and the compound as a whole is neutral.

The shortest metal–ligand bond is to the coordinated water molecule (2.184 Å), followed by the amino nitrogen of monoethanolamine (2.240 Å) and its hydroxyl oxygen (2.307 Å). The three bonds to the amide nitrogen atoms are markedly longer, at 2.361, 2.445 and 2.543 Å, about a mean of 2.450 Å. Such distances are long even for high-spin manganese(II), in which the absence of ligand-field stabilization permits relatively long and deformable metal–ligand bonds, and the longest of them approaches the limit of what may reasonably be described as a coordinate bond. A bond-valence-sum calculation over the six donors gives 1.54 valence units, appreciably below the value of 2 expected for a divalent center, indicating that the manganese ion is underbonded in this coordination environment.

The coordination polyhedron is severely distorted. The three approximately trans angles are 156.67, 154.02 and 147.84°, deviating from linearity by 23 to 32°, while the remaining angles range from 71.92 to 130.79°, the smallest corresponding to the constrained bite of the monoethanolamine chelate. The geometry is therefore better described as a strongly distorted octahedron approaching trigonal-prismatic character than as a regular one. Distortion of this magnitude is possible because a high-spin d^5 configuration offers no electronic preference for any particular polyhedron, so that the arrangement is governed by the steric requirements of three bulky aryl amides and by the weakness of the metal–amide interaction itself.

The geometry of the amide groups is itself informative. The amide C–N distances (mean 1.404 Å) are markedly longer than the value of approximately 1.33 Å expected for an unperturbed primary aromatic amide, while the C=O distances (mean 1.230 Å) are close to the normal value. This pattern indicates a loss of amide resonance: donation of the nitrogen lone pair to the metal removes it from conjugation with the carbonyl group, which in turn acquires increased double-bond character. The three phenolic hydroxyl groups occupy the para positions of the aromatic rings, are geometrically incapable of reaching the metal center, and are not coordinated; together with the chloride ions and the coordinated water molecule, they participate in an extensive intermolecular hydrogen-bonding network.

As set out in X-ray diffraction measurement and structural modeling, these geometric parameters derive from the DFT-optimized model refined as a rigid body against the powder profile, and are not independently determined by the diffraction experiment. Two limitations follow. First, nitrogen and oxygen scatter X-rays almost identically at this resolution, so the diffraction data cannot discriminate between the two; the donor assignment rests on the computational model and on the spectroscopic evidence discussed above. Second, coordination of a neutral primary amide through nitrogen rather than through the carbonyl oxygen is uncommon, since the nitrogen lone pair is normally delocalized into the C=O π system. The N-coordinated geometry reported here is a true minimum on the calculated potential energy surface

and is consistent with the observed profile, but we do not regard the diffraction data alone as sufficient to establish it in preference to an O-coordinated alternative.

Table 1. Crystallographic and Rietveld refinement data for $[Mn(4\text{-}OHBA)_3(MEA)(H_2O)]Cl_2$.

Parameter	Value
Empirical formula	$C_{23}H_{30}Cl_2MnN_4O_8$
Formula weight	616.35
Temperature	298 K
Radiation, wavelength	Cu Kα, 1.54186 Å
Measurement geometry	Gandolfi attachment, capillary mount
Crystal system	Triclinic
Space group	P-1 (No. 2)
a, b, c (Å)	10.950(4), 11.896(7), 10.00(18)
α, β, γ (°)	100.93(3), 93.62(3), 90.17(5)
V (Å³)	1277(23)
Z	2
ρcalc (g cm^{-3})	1.604
μ (Cu Kα) (mm^{-1})	6.629
F(000)	638
2θ range (°), step	5.0–60.0, 0.01
Data points	5501
Bragg reflections	735
dmin (Å)	1.537
Refinement method	Rietveld, rigid-body model
Refined parameters	42
Preferred orientation	Spherical harmonics, order 2
Rp, Rwp, Rexp	0.0404, 0.0549, 0.0439
Goodness of fit (Rwp/Rexp)	1.251
RI (Bragg intensity residual)	0.0089
CCDC deposition number	2575511

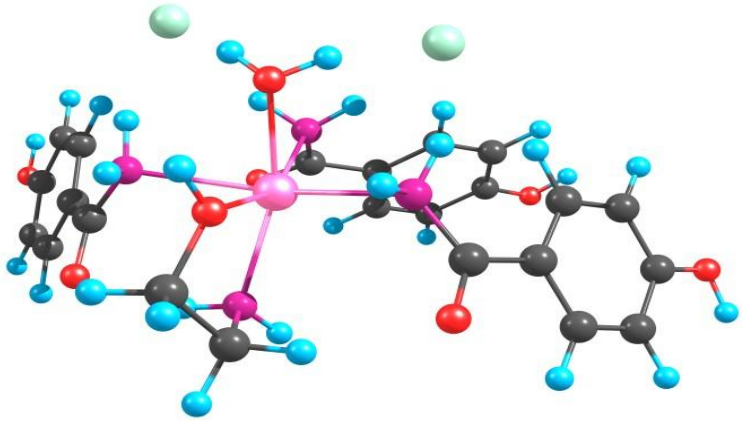

Figure 3. Molecular model of the $[Mn(4\text{-}OHBA)_3(MEA)(H_2O)Cl_2]$.

The packing is illustrated in Figure 4. The complex cations stack in layers, with the chloride ions occupying the space between them, so that the structure alternates between organic and ionic regions. The shortest Mn···Mn separation is 7.03 Å, the metal centers being held apart by the bulk

of the three benzamide ligands, and there is no indication of any direct metal–metal interaction. The chloride ions are anchored by hydrogen bonds to the oxygen and nitrogen donors of neighboring cations: Cl2 lies 2.88 Å from a phenolic oxygen, 3.42 Å from the hydroxyl oxygen of monoethanolamine and 3.46 Å from an amide nitrogen, while Cl1 makes a longer contact of 3.24 Å to a second phenolic oxygen. The para-hydroxyl groups, which take no part in coordination, therefore have a structural role in binding the counter-ions and linking adjacent layers.

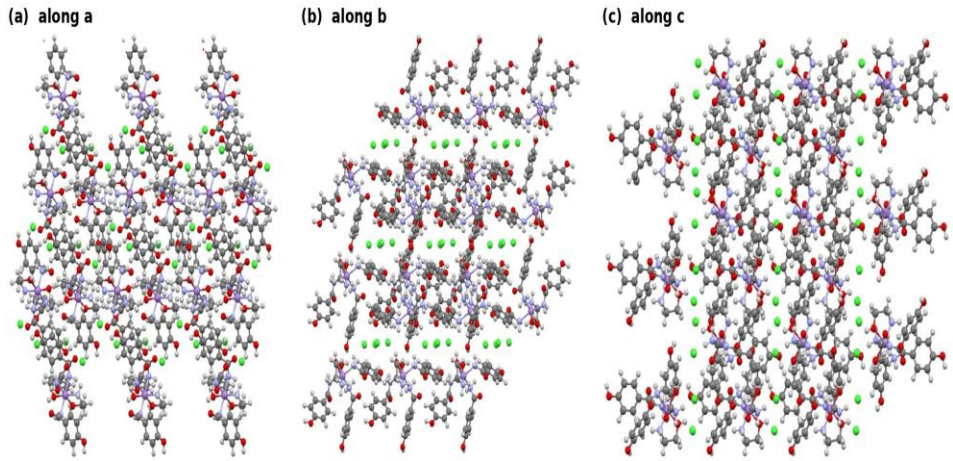

Figure 4. Crystal packing of $[Mn(4\text{-}OHBA)_3(MEA)(H_2O)]Cl_2$ viewed along (a) the a axis, (b) the b axis and (c) the c axis. Manganese is shown in purple, chloride in green, oxygen in red and nitrogen in blue. Hydrogen atoms are included.

Frontier molecular orbital and TD-DFT analysis

Frontier molecular orbital analysis was performed in order to characterize the electronic structure and electron-transfer properties of the complex. Because the ground state is a spin sextet, the calculation is unrestricted, and the two spin manifolds must be considered separately. In the α manifold, the highest occupied and lowest unoccupied orbitals lie at −6.001 and −1.813 eV, giving a gap of 4.188 eV; in the β manifold, the corresponding values are −6.165 and −1.913 eV, giving 4.252 eV. The two frontier orbitals are shown in Figure 5 (a). The highest occupied orbital of the system as a whole is therefore the α-HOMO and the lowest unoccupied orbital is the β-LUMO, separated by 4.088 eV. We note that this last quantity spans two spin manifolds and does not correspond to any spin-allowed transition; it is quoted only for comparison with values reported elsewhere on the same convention. That the lowest unoccupied orbital belongs to the minority-spin manifold is expected for a high-spin d^5 configuration, in which all five α-d orbitals are occupied, and the empty metal d orbitals lie in the β manifold. The calculated gaps are of the same order as those reported by Mohammed and co-workers for a related series of mixed-ligand complexes [33].

Time-dependent density functional theory calculations [34] were performed at the same level of theory in order to characterize the electronic excitations. The calculated absorption spectrum is presented in Figure 5 (b), showing both the discrete vertical transitions and the simulated envelope obtained by Gaussian broadening.

The calculated gap is considerably larger than the energies typical of d–d transitions in manganese(II) complexes, which generally fall between 1.5 and 2.5 eV. Ligand-field transitions

in high-spin d^5 systems are moreover spin-forbidden, requiring a change of multiplicity from the sextet ground state, and are correspondingly weak. The intense calculated transitions in the ultraviolet region are therefore unlikely to be ligand-field in origin. On the basis of the calculated oscillator strengths and of the composition of the orbitals involved, the dominant transition is assigned to a charge-transfer process in which electron density is displaced from ligand-based orbitals towards the manganese center.

We note two caveats. First, the HOMO–LUMO gap and the vertical excitation energy are distinct quantities, and the numerical proximity of the gap to the calculated absorption maximum should not be taken as mutual confirmation; the correspondence is a consequence of the transition being dominated by the HOMO→LUMO configuration, not independent evidence for it. Second, a secure assignment of charge-transfer character requires quantitative orbital analysis. The assignment offered here rests on the calculated oscillator strengths and on the spatial distribution of the orbitals involved, and should be regarded as provisional pending a fragment-contribution or natural transition orbital analysis.

Natural bond orbital analysis of the optimized sextet provides an independent description of the metal center. The natural charge on manganese is +1.641, and the natural electron configuration is [core]4s(0.22)3d(5.12)4p(0.02), corresponding to a d^5 ion that has accepted approximately 0.36 electrons of ligand donation. The spin density on manganese is 4.860 of a total of 5.000, so that 97 per cent of the unpaired electron density resides on the metal, with only small positive contributions on the donor atoms (0.006–0.026). These values confirm a localized high-spin manganese(II) center and are consistent with the spin-state energetics.

Metal-to-ligand charge transfer is considered less probable for this system, since such transitions require low-lying π* acceptor orbitals of the kind found in strongly π-accepting ligands such as 2,2′-bipyridine or 1,10-phenanthroline. The π* orbitals of 4-hydroxybenzamide are expected to lie too high in energy to serve as effective acceptors, and the relatively high oxidation potential of manganese(II) makes it a poor electron donor in this context.

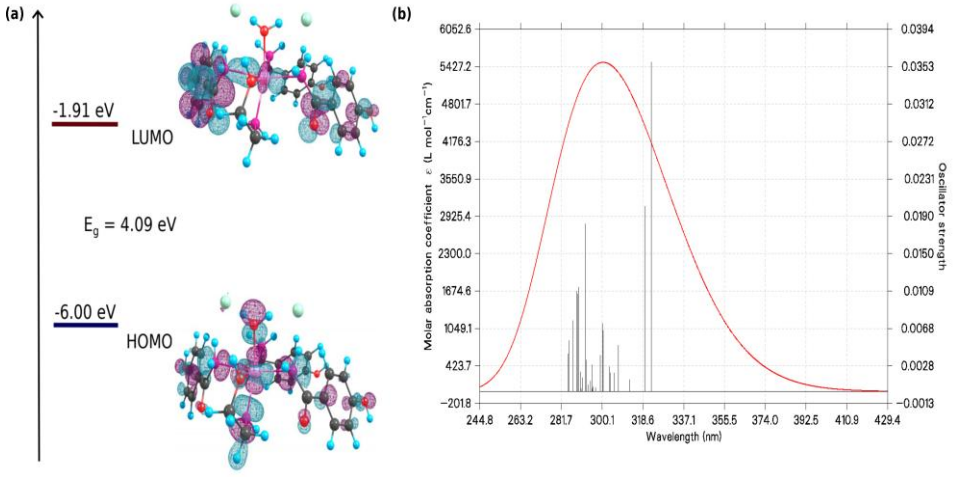

Figure 5. (a) Frontier molecular orbitals of $[Mn(4\text{-}OHBA)_3(MEA)(H_2O)]Cl_2$ (isovalue 0.02 a.u.), (b) Calculated UV–Vis absorption spectrum of $[Mn(4\text{-}OHBA)_3(MEA)(H_2O)]Cl_2$ obtained by TD-DFT, showing the discrete vertical transitions and the Gaussian-broadened envelope.

Global reactivity descriptors

Global reactivity descriptors provide quantitative insight into the chemical reactivity and stability of molecular systems. Although these may be estimated from frontier orbital energies by way of Koopmans' theorem [35], a more rigorous approach is to calculate the adiabatic ionization potential and electron affinity by explicit optimization of the charged species [36,37]. The adiabatic approach was adopted here.

Separate geometry optimizations were performed for the neutral complex (charge 0, multiplicity 6), the oxidized cation (charge +1, multiplicity 5) and the reduced anion (charge −1, multiplicity 5), each at the TPSSh/Def2-SVP/CPCM level. The adiabatic ionization potential was obtained as the energy difference between the optimized cation and the neutral species, and the adiabatic electron affinity from the difference between the neutral species and the optimized anion. The resulting values were 5.77 and 2.39 eV respectively.

From these quantities the remaining descriptors follow within the framework of conceptual density functional theory. The Mulliken electronegativity is the arithmetic mean of the ionization potential and the electron affinity,

$$\chi = (IP + EA)/2 \quad (1)$$

giving 4.08 eV. The chemical potential is the negative of this quantity, $\mu = -(IP + EA)/2 = -4.08$ eV. The chemical hardness, which measures resistance to charge transfer,

$$\eta = (IP - EA)/2 \quad (2)$$

is 1.69 eV; the softness $S = 1/(2\eta)$ is 0.296 eV^{-1}; and the electrophilicity index

$$\omega = \chi^2/(2\eta) \quad (3)$$

is 4.92 eV. The descriptors are collected in Table 2. Taken together they describe a species of moderate hardness, and therefore of reasonable stability towards charge perturbation, combined with appreciable electrophilic character. Within the hard–soft acid–base framework the intermediate hardness suggests that the complex may engage with both harder and softer reaction partners.

Table 2. Global reactivity descriptors for $[Mn(4\text{-}OHBA)_3(MEA)(H_2O)]Cl_2$.

Descriptor	Symbol	Definition	Value
Ionisation potential	IP	E(cation) − E(neutral)	5.77 eV
Electron affinity	EA	E(neutral) − E(anion)	2.39 eV
Electronegativity	χ	(IP + EA)/2	4.08 eV
Chemical potential	μ	−(IP + EA)/2	−4.08 eV
Chemical hardness	η	(IP − EA)/2	1.69 eV
Chemical softness	S	$1/(2\eta)$	0.296 eV^{-1}
Electrophilicity index	ω	$\chi^2/(2\eta)$	4.92 eV

Molecular docking

Molecular docking was performed against human apurinic/apyrimidinic endonuclease 1, an enzyme central to the base excision repair pathway and to redox regulation [38, 39]. The enzyme is frequently overexpressed in human cancers and is associated with resistance to chemotherapy and with poor prognosis, which has made it a target of interest in anticancer drug development [40, 41].

Receptor preparation and binding-site identification

The crystal structure of human apurinic/apyrimidinic endonuclease 1 was obtained from the Protein Data Bank [42]. The deposited coordinates comprise residues 44–318, corresponding to the catalytic domain; the disordered N-terminal segment is absent. The structure had been solved using heavy-atom derivatives, and the platinum and samarium ions used for phasing, together with the crystallographic water molecules, were removed before docking, since they are artifacts of structure determination rather than components of the enzyme. Two residues that the deposited file recorded as heterogroups were restored to the polypeptide, giving a continuous chain of 275 residues.

Docking was performed in cavity-detection-guided blind mode: rather than assuming the location of the binding site, the whole receptor surface was surveyed, candidate cavities were detected from the protein-surface curvature using the CurPocket algorithm implemented in CB-Dock2 [43] and ranked by volume, and each was then docked independently. Five cavities were identified. The largest, of volume 571 Å^3, is lined by Asn68, Asp70, Glu96, Tyr128, Tyr171, Asn174, Arg177, Asp210, Asn212, Asn226, Asn229, Ala230, Gly231, Phe266, Thr268, Met270, Trp280, Leu282, Asp308 and His309, and therefore corresponds to the catalytic pocket; the remaining four, of 212, 177, 119 and 107 Å^3, lie elsewhere on the protein surface. Two independent checks support this assignment. The centroid of the catalytic and basic-site-binding residues lies 5.2 Å from the center of this cavity, and the samarium ion that occupies the catalytic divalent-metal site in the crystal structure lies 5.4 Å from it, while the remaining phasing ions are 19–37 Å away. Docking was carried out in a box centered at (28.55, −11.72, 20.05) enclosing this cavity.

Docking protocol

Docking was carried out with CB-Dock2 [43], which couples the CurPocket cavity-detection step described above to pose generation and scoring with AutoDock Vina [44]. Each detected cavity was docked independently under the cavity-detection-guided blind protocol described above, so that the preferred binding site emerged from the calculation rather than being imposed. The DFT-optimised sextet ground-state geometry of the complex was used as the ligand, docked as the dication $[Mn(4\text{-}OHBA)_3(MEA)(H_2O)]^{2+}$ with both chloride ions removed, since the counter-ions are not expected to remain associated with the complex in aqueous solution at physiological pH. Free 4-hydroxybenzamide was docked into the same receptor and the same cavity under otherwise identical conditions, so that the complex and its principal ligand could be compared directly. The search box was automatically scaled to the ligand, giving edge lengths of 23 Å for the complex and 17 Å for the free ligand; this difference is noted for completeness, although the scoring of a given pose does not depend on box size. Poses were ranked by the Vina scoring function, and the top-ranked pose in each cavity was retained for analysis.

Interactions were analyzed from the retained poses using a heavy-atom cutoff of 4.5 Å for contacts and 3.5 Å between nitrogen or oxygen atoms for hydrogen bonds. Solvent-accessible surface areas were computed by the Shrake–Rudolph algorithm with a probe radius of 1.4 Å, both for the isolated ligand and for the ligand within the complex, the difference giving the surface buried on binding.

Binding affinity and site selectivity

The top-ranked poses of both species in the catalytic cavity are shown in Figure 6 (a) and (b). Quantitative parameters derived from the docking analysis reflect distinct binding behaviors for $[Mn(4\text{-}OHBA)_3(MEA)(H_2O)]^{2+}$ and free 4-hydroxybenzamide. In the catalytic pocket (cavity 1), the complex bound with a predicted affinity of −9.1 kcal mol^{-1}, ahead of the two alternative

pockets at −8.3 and −7.3 kcal mol^{-1}. Free 4-hydroxybenzamide showed no preference among the cavities, with predicted affinities of −5.3, −5.4, and −4.3 kcal mol^{-1} across cavities 1, 2, and 3, respectively, rendering the catalytic site and the second cavity indistinguishable within the scoring function's resolution.

Structural and surface interaction measurements further illustrate these differences. The complex contains 36 heavy atoms, engages 15 residues within 4.5 Å, forms 5 hydrogen bonds (involving Asp210, Thr268, Asn212, Asn226, and His309), and buries 382 Å^2 of solvent-accessible surface on binding (77% total surface, with a mean burial per heavy atom of 68%). In contrast, free 4-hydroxybenzamide comprises 10 heavy atoms, contacts 11 residues within 4.5 Å, forms 6 hydrogen bonds (engaging Asn212, Glu96, Asp308, Asp70, Asn174, and Asn68), and buries 169 Å^2 of surface (74% total surface, with a mean heavy-atom burial of 78%).

This difference in selectivity is, in our view, the more informative result. The absolute scores of the two species are not strictly comparable, because empirical scoring functions of this type scale with molecular size, and the complex contains 36 heavy atoms against 10 in the free ligand. Expressed per heavy atom the free ligand is in fact the more efficient binder, at 0.53 against 0.25 kcal mol^{-1} per atom. The ranking of cavities by a single species against itself, however, is not affected by this scaling, and on that measure the assembled complex discriminates in favor of the catalytic pocket where the free ligand does not.

Binding modes

Within the catalytic cavity, the two species occupy overlapping but distinct subsites as shown in Figures 6 (c) and (d) and Figure 7. Seven residues contact both: Tyr171, Asn174, Asp210, Asn212, Phe266, Leu282 and His309. Beyond this shared core, the two diverge. Free 4-hydroxybenzamide penetrates to the floor of the pocket, hydrogen bonding to Asn212 (2.77 Å), Glu96 (2.86 Å), Asp308 (2.90 Å), Asp70 (3.09 Å), Asn174 (3.18 Å) and Asn68 (3.18 Å) — the residues that constitute the catalytic metal-binding and basic-site-recognition machinery. The complex, being considerably larger, cannot reach that depth; it sits higher in the cleft and extends towards Arg177, Val213, Asn226, Asn229, Ala230, Gly231, Thr268 and Trp280, forming hydrogen bonds with Asp210 (2.93 Å), Thr268 (2.95 Å), Asn212 (2.98 Å), Asn226 (3.05 Å) and His309 (3.32 Å).

Both binding modes therefore engage the catalytic triad of Asp210, Asn212 and His309, but by different routes: the free ligand from within the pocket and the complex across its mouth. The manganese center, bearing a formal charge of +2, is expected to contribute an electrostatic component to the interaction with the aspartate residues lining the site.

Surface burial follows the same pattern (Figure 7). The complex buries 382 Å^2 of its 496 Å^2 solvent-accessible surface on binding, corresponding to 77 percent, against 169 Å^2 of 229 Å^2 (74 percent) for the free ligand. The two species thus bury a similar fraction of their surface, but the complex buries more than twice the absolute area. Examined atom by atom, however, the distributions differ: every heavy atom of the free ligand is substantially desolvated, with a mean burial of 78 percent, whereas the complex retains a subset of atoms — belonging to the peripheral benzamide arms — that remain almost fully solvent-exposed, giving a lower mean of 68 percent. This incomplete desolvation of the periphery accounts for the lower binding efficiency per atom noted above.

The binding modes described here suggest that both species may occupy the substrate-binding region and impede access of damaged DNA to the active site. We emphasize that these are computational predictions alone. Docking scores are estimates produced by an empirical function and are not measurements of affinity; we therefore make no comparison between the values obtained here and the inhibitory concentrations reported for established inhibitors such as CRT0044876 [45] or AR03 [46], which were determined experimentally and under conditions not comparable to ours. No biological activity has been measured for the present compound.

Enzymatic inhibition assays and cell-based studies would be required before any conclusion regarding biological or therapeutic potential could be drawn, and alternative modes of interaction, including redox activity at the metal center, cannot be excluded.

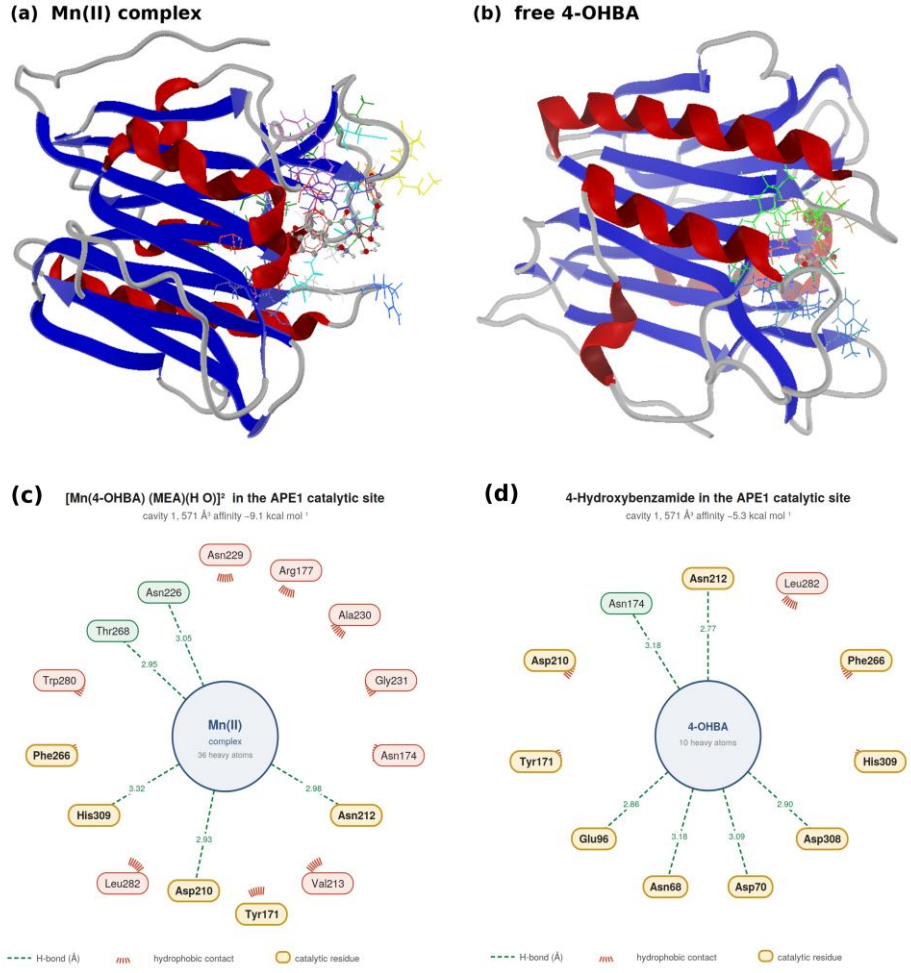

Figure 6. Top-ranked docked poses in the catalytic site of human APE1: (a) $[Mn(4\text{-}OHBA)_3(MEA)(H_2O)]^{2+}$, (b) free 4-hydroxybenzamide, (c) two-dimensional interaction diagrams for the top-ranked poses in the catalytic cavity for $[Mn(4\text{-}OHBA)_3(MEA)(H_2O)]^{2}$ and (d) two-dimensional interaction diagrams for the top-ranked poses in the catalytic cavity for free 4-hydroxybenzamide. The enzyme is shown as a cartoon with helices in red, strands in blue, and loops in grey; the ligand is shown as ball-and-stick, and the residues lining the binding site as colored sticks.

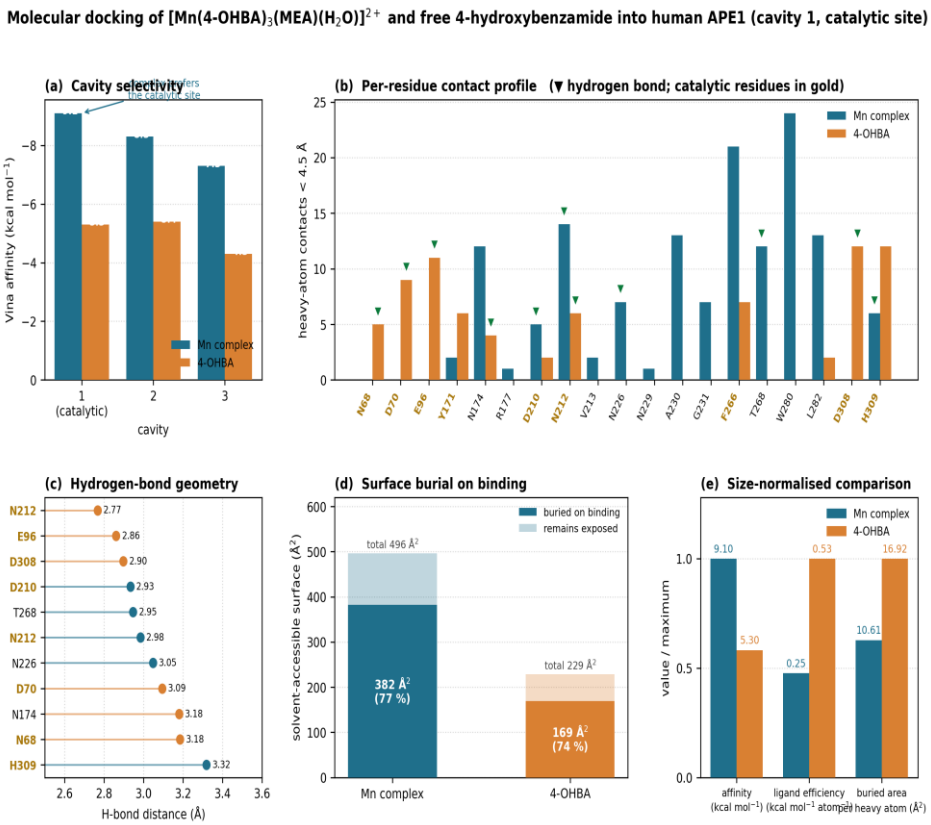

Figure 7. Quantitative comparison of the two docked species: (a) predicted affinity in each of the three largest cavities; (b) heavy-atom contacts per residue, hydrogen bonds marked with triangles and catalytic residues labeled in gold; (c) hydrogen-bond distances; (d) solvent-accessible surface buried on binding; (e) size-normalized comparison of affinity, ligand efficiency and buried area per heavy atom.

CONCLUSION

A new mixed-ligand manganese(II) compound, $[Mn(4\text{-}OHBA)_3(MEA)(H_2O)]Cl_2$, has been prepared and characterized by a combination of spectroscopic, microscopic, diffraction and computational methods. X-ray powder diffraction data, collected in Gandolfi geometry and analyzed by Rietveld refinement, index on a triclinic cell in space group P-1 with two formula units per cell. A molecular model derived from density functional theory refines satisfactorily against the observed profile and describes a mononuclear complex in which manganese(II) occupies a distorted octahedral N_4O_2 environment, with the two chloride ions in the outer coordination sphere. Infrared spectroscopy is consistent with this description, indicating chelation of monoethanolamine through nitrogen and oxygen and involvement of the amide group of 4-hydroxybenzamide in coordination. No corresponding entry was found in the Cambridge Structural Database. We emphasize that the molecular geometry reported here is a computational model shown to be compatible with the diffraction data, and not an independent experimental determination; confirmation would require single-crystal diffraction or, at minimum, powder data

of higher quality collected from a bulk polycrystalline sample. Density functional theory calculations establish a high-spin sextet ground state, well separated from the quartet and doublet configurations, as expected for a d^5 center in a weak ligand field. Analysis of the frontier orbitals and of the time-dependent DFT excitation spectrum indicates that the lowest intense transition has substantial charge-transfer character. The global reactivity descriptors describe a species of moderate chemical hardness with appreciable electrophilicity. Molecular docking against human apurinic/apyrimidinic endonuclease 1 predicts favourable binding within the catalytic pocket, identified independently by cavity detection and confirmed by the position of the catalytic residues and of the metal site observed crystallographically. The complex binds most strongly in this cavity and discriminates in its favor, whereas free 4-hydroxybenzamide shows no preference among the available pockets; both engage the catalytic triad, though from different subsites. These results are computational predictions only, and the absolute scores are not strictly comparable between species of different size. No biological activity has been measured, and enzymatic inhibition assays together with cell-based studies would be required before any conclusion about the therapeutic potential of this compound could be drawn.

ACKNOWLEDGMENT

We would like to thank to Gdansk University of Technology CI-TASK for providing high speed computing power.

Funding statement: This research was supported by the State Budget of the Republic of Uzbekistan

Data availability: Crystallographic data have been deposited with the Cambridge Crystallographic Data Centre, deposition number CCDC 2575511, and may be obtained free of charge at www.ccdc.cam.ac.uk/structures. The checkCIF/PLATON report is supplied as Supporting Information.

Conflicts of interest: The authors declare no conflicts of interest.

REFERENCES

1. Umena, Y.; Kawakami, K.; Shen, J.R.; Kamiya, N. Crystal structure of oxygen-evolving photosystem II at a resolution of 1.9 Å. *Nature* **2011**, 473, 55-65.
2. Jin, L.; Smith, P.; Noble, C.J.; Stranger, R.; Hanson, G.R.; Pace, R.J. Electronic structure of the oxygen evolving complex in photosystem II, as revealed by 55Mn davies ENDOR studies at 2.5 K. *Phys. Chem. Chem. Phys.* **2014**, 16, 7799-7812.
3. Law, N.A.; Caudle, M.T.; Pecoraro, V.L. Manganese redox enzymes and model systems: Properties, structures, and reactivity. *Adv. Inorg. Chem.* **1998**, 46, 305-440.
4. Signorella, S.; Hureau, C. Bioinspired functional mimics of the manganese catalases. *Coord. Chem. Rev.* **2012**, 256, 1229-1245.
5. Gauuan, P.J.F.; Trova, M.P.; Boros, L.G.; Bocckino, S.B.; Crapo, J.D. Superoxide dismutase mimetics: synthesis and structure-activity relationship study of MnTBAP analogues. *Bioorg. Med. Chem.* **2002**, 10, 3013-3021.
6. Peña, O.; Gutiérrez, D.; Durán, P.; Moure, C. Magnetic properties of manganese-site substituted Y(Cu, Mn)O_3. *Bol. Soc. Esp. Ceram. Vidr.* **2003**, 42, 295-300.
7. Li, X.; Li, B.; Hu, Z.; Cheng, H.; Zhao, Q.; Chen, Z. Structural and magnetic properties of manganese and nickel clusters with 9,10-phenanthrenedione-9-oxime ligands. *Trans. Met. Chem.* **2017**, 42, 503-510.

8. Lu, L.; Wang, J.; Wu, W.P.; Wu, X.R.; Kumar, A. Synthesis, Hirshfeld surface analyses and magnetism of a 1D Mn(II) complex. *Bull. Chem. Soc. Ethiop.* **2016**, 30, 111-118.
9. Glerup, J.; Goodson, P.A.; Hodgson, D.J.; Michelsen, K.; Rychlewska, U.; Weihe, H. Synthesis and characterization of monomeric and dimeric manganese(II) and zinc(II) complexes of pyridine-2-carbaldoxime. *Bull. Chem. Soc. Ethiop.* **2000**, 14, 129-141.
10. Yu, M.; Ambrose, S.L.; Whaley, Z.L.; Fan, S.; Gorden, J.D.; Beyers, R.J.; Goldsmith, C.R. A mononuclear manganese(II) complex demonstrates a strategy to simultaneously image and treat oxidative stress. *J. Am. Chem. Soc.* **2014**, 136, 12836-12839.
11. Siqueira, J.D.; Sokolovicz, Y.C.A.; Oliveira, M.M.; Martins, F.M.; Loreto, M.F.; dos Santos Siqueira, F.; Back, D.F. High antioxidant and antibiofilm activity of manganese (II and III) complexes derived from pyridoxal and aromatic hydrazides. *J. Inorg. Biochem.* **2025**, 276, 113166.
12. Zhou, D.F.; Chen, Q.Y.; Qi, Y.; Fu, H.J.; Li, Z.; Zhao, K.D.; Gao, J. Anticancer activity, attenuation on the absorption of calcium in mitochondria, and catalase activity for manganese complexes of N-substituted di(picolyl) amine. *Inorg. Chem.* **2011**, 50, 6929-6937.
13. Li, M.X.; Chen, C.L.; Zhang, D.; Niu, J.Y.; Ji, B.S. Mn(II), Co(II) and Zn(II) complexes with heterocyclic substituted thiosemicarbazones: Synthesis, characterization, X-ray crystal structures and antitumor comparison. *Eur. J. Med. Chem.* **2010**, 45, 3169-3177.
14. Dorkov, P.; Pantcheva, I.N.; Sheldrick, W.S.; Mayer-Figge, H.; Petrova, R.; Mitewa, M. Synthesis, structure and antimicrobial activity of manganese(II) and cobalt(II) complexes of the polyether ionophore antibiotic sodium monensin A. *J. Inorg. Biochem.* **2008**, 102, 26-32.
15. Barmpa, A.; Frousiou, O.; Kalogiannis, S.; Perdih, F.; Turel, I.; Psomas, G. Manganese(II) complexes of the quinolone family member flumequine: Structure, antimicrobial activity and affinity for albumins and calf-thymus DNA. *Polyhedron* **2018**, 145, 166-175.
16. Singh, D.P.; Kumar, K.; Sharma, C. New 14-membered octaazamacrocyclic complexes: Synthesis, spectral, antibacterial and antifungal studies. *Eur. J. Med. Chem.* **2010**, 45, 1230-1236.
17. Zampakou, M.; Balala, S.; Perdih, F.; Kalogiannis, S.; Turel, I.; Psomas, G. Structure, antimicrobial activity, albumin- and DNA-binding of manganese(II)-sparfloxacinato complexes. *RSC Adv.* **2015**, 5, 11861-11872.
18. Dimiza, F.; Raptopoulou, C.P.; Psycharis, V.; Papadopoulos, A.N.; Psomas, G. Manganese(II) complexes with the non-steroidal anti-inflammatory drugs naproxen and mefenamic acid: Synthesis, structure, antioxidant capacity, and interaction with albumins and DNA. *New J. Chem.* **2018**, 42, 16666-16681.
19. Shen, F.; Cai, W.S.; Li, J.L.; Feng, Z.; Cao, J.; Xu, B. The association between deficient manganese levels and breast cancer: A meta-analysis. *Int. J. Clin. Exp. Med.* **2015**, 8, 3671-3680.
20. Manuja, R.; Sachdeva, S.; Jain, A.; Chaudhary, J. A comprehensive review on biological activities of p-hydroxybenzoic acid and its derivatives. *Int. J. Pharm. Sci. Rev. Res.* **2013**, 22, 109-115.
21. Kamaya, Y.; Tsuboi, S.; Takada, T.; Suzuki, K. Growth stimulation and inhibition effects of 4-hydroxybenzoic acid and some related compounds on the freshwater green alga *Pseudokirchneriella subcapitata*. *Arch. Environ. Contam. Toxicol.* **2006**, 51, 537-544.
22. Cho, J.-Y.; Moon, J.-H.; Seong, K.-Y.; Park, K.-H. Antimicrobial activity of 4-hydroxybenzoic acid and trans-4-hydroxycinnamic acid isolated and identified from rice hull. *Biosci. Biotechnol. Biochem.* **1998**, 62, 2273-2276.
23. Ibragimov, A.B.; Ashurov, Zh.M.; Zakirov, B.S. Molecular and crystal structure of a mixed-ligand cadmium complex with p-hydroxybenzoic acid and monoethanolamine. *J. Struct. Chem.* **2017**, 58, 588-590.
24. Nakamoto, K. *Infrared and Raman Spectra of Inorganic and Coordination Compounds*, 6th ed., Wiley: New York; **2009**; p 310.

25. Frisch, M.J.; Trucks, G.W.; Schlegel, H.B.; Scuseria, G.E.; Robb, M.A.; Cheeseman, J.R.; Scalmani, G.; Barone, V.; Petersson, G.A.; Nakatsuji, H.; Li, X.; Caricato, M.; Marenich, A.V.; Bloino, J.; Janesko, B.G.; Gomperts, R.; Mennucci, B.; Hratchian, H.P.; Ortiz, J.V.; Izmaylov, A.F.; Sonnenberg, J.L.; Williams-Young, D.; Ding, F.; Lipparini, F.; Egidi, F.; Goings, J.; Peng, B.; Petrone, A.; Henderson, T.; Ranasinghe, D.; Zakrzewski, V.G.; Gao, J.; Rega, N.; Zheng, G.; Liang, W.; Hada, M.; Ehara, M.; Toyota, K.; Fukuda, R.; Hasegawa, J.; Ishida, M.; Nakajima, T.; Honda, Y.; Kitao, O.; Nakai, H.; Vreven, T.; Throssell, K.; Montgomery, J.A., Jr.; Peralta, J.E.; Ogliaro, F.; Bearpark, M.J.; Heyd, J.J.; Brothers, E.N.; Kudin, K.N.; Staroverov, V.N.; Keith, T.A.; Kobayashi, R.; Normand, J.; Raghavachari, K.; Rendell, A.P.; Burant, J.C.; Iyengar, S.S.; Tomasi, J.; Cossi, M.; Millam, J.M.; Klene, M.; Adamo, C.; Cammi, R.; Ochterski, J.W.; Martin, R.L.; Morokuma, K.; Farkas, O.; Foresman, J.B.; Fox, D.J. *Gaussian 16*, Revision C.01, Gaussian, Inc.: Wallingford, CT, **2016**.
26. Tao, J.; Perdew, J.P.; Staroverov, V.N.; Scuseria, G.E. Climbing the density functional ladder: Nonempirical meta-generalized gradient approximation designed for molecules and solids. *Phys. Rev. Lett.* **2003**, 91, 146401.
27. Staroverov, V.N.; Scuseria, G.E.; Tao, J.; Perdew, J.P. Comparative assessment of a new nonempirical density functional: Molecules and hydrogen-bonded complexes. *J. Chem. Phys.* **2003**, 119, 12129-12137.
28. Weigend, F.; Ahlrichs, R. Balanced basis sets of split valence, triple zeta valence and quadruple zeta valence quality for H to Rn: Design and assessment of accuracy. *Phys. Chem. Chem. Phys.* **2005**, 7, 3297-3305.
29. Jensen, K.P. Bioinorganic chemistry modeled with the TPSSh density functional. *Inorg. Chem.* **2008**, 47, 10357-10365.
30. Blomberg, M.; Siegbahn, P.A. A comparative study of high-spin manganese and iron complexes. *Theor. Chem. Acc.* **1997**, 97, 72-79.
31. Bacciu, D.; Chen, C.H.; Surawatanawong, P.; Foxman, B.M.; Ozerov, O.V. High-spin manganese(II) complexes of an amido/bis(phosphine) PNP ligand. *Inorg. Chem.* **2010**, 49, 5328-5334.
32. Conradie, J. Redox chemistry of bis(terpyridine)manganese(II) complexes – a molecular view. *J. Electroanal. Chem.* **2022**, 913, 116272.
33. Mohammed, E.H.; Mohammed, E.R.; Yahya, E.M.; Alsultan, M. Synthesis, characterization, DFT study and biological evaluation of complexes derived from transition metal and mixed ligands. *Inorganics* **2025**, 13, 334.
34. Schirmer, J. Review of the foundations of time-dependent density-functional theory (TDDFT). *Phys. Chem. Chem. Phys.* **2025**, 27, 4992-5005.
35. Zhan, C.G.; Nichols, J.A.; Dixon, D.A. Ionization potential, electron affinity, electronegativity, hardness, and electron excitation energy: Molecular properties from density functional theory orbital energies. *J. Phys. Chem. A* **2003**, 107, 4184-4195.
36. Ibragimov, S.; Komando, L. Standard redox potential of [Co(bpy)3]2+/3+ and [Co(phen)3]2+/3+ redox couples using a density functional theory protocol. *Struct. Chem.* **2026**, 37, 481-494.
37. Ibragimov, S.; Komando, L.; Bobrowski, M. Isomers of iron(III) oxides and cobalt(III) oxides and their redox properties: Quantum-chemical insights. *Molecules* **2025**, 30, 4158.
38. Mol, C.D.; Izumi, T.; Mitra, S.; Tainer, J.A. DNA-bound structures and mutants reveal abasic DNA binding by APE1 DNA repair and coordination. *Nature* **2000**, 403, 451-456.
39. Kelley, M.R.; Georgiadis, M.M.; Fishel, M.L. APE1/Ref-1 role in redox signaling: Translational applications of targeting the redox function of the DNA repair/redox protein APE1/Ref-1. *Antioxid. Redox Signal.* **2012**, 17, 1767-1806.
40. Abbotts, R.; Madhusudan, S. Human AP endonuclease 1 (APE1): From mechanistic insights to druggable target in cancer. *Cancer Treat. Rev.* **2010**, 36, 425-435.

41. Fishel, M.L.; Kelley, M.R. The DNA base excision repair protein Ape1/Ref-1 as a therapeutic and chemopreventive target. *Mol. Aspects Med.* **2007**, 28, 375-395.
42. Berman, H.M.; Westbrook, J.; Feng, Z.; Gilliland, G.; Bhat, T.N.; Weissig, H.; Shindyalov, I.N.; Bourne, P.E. The protein data bank. *Nucleic Acids Res.* **2000**, 28, 235-242.
43. Liu, Y.; Yang, X.; Gan, J.; Chen, S.; Xiao, Z.-X.; Cao, Y. CB-Dock2: Improved protein ligand blind docking by integrating cavity detection, docking and homologous template fitting. *Nucleic Acids Res.* **2022**, 50, W159-W164.
44. Trott, O.; Olson, A.J. AutoDock Vina: improving the speed and accuracy of docking with a new scoring function, efficient optimization, and multithreading. *J. Comput. Chem.* **2010**, 31, 455-461.
45. Madhusudan, S.; Smart, F.; Shrimpton, P.; Parsons, J.L.; Gardiner, L.; Houlbrook, S.; Talbot, D.C.; Hammonds, T.; Freemont, P.A.; Sternberg, M.J.E.; Dianov, G.L.; Hickson, I.D. Isolation of a small molecule inhibitor of DNA base excision repair. *Nucleic Acids Res.* **2005**, 33, 4711-4724.
46. Bapat, A.; Glass, L.S.; Luo, M.; Fishel, M.L.; Long, E.C.; Georgiadis, M.M.; Kelley, M.R. Novel small-molecule inhibitor of apurinic/apyrimidinic endonuclease 1 blocks proliferation and reduces viability of glioblastoma cells. *J. Pharmacol. Exp. Ther.* **2010**, 334, 988-998.